Science
AAAS

Supplementary Materials for

State dependence of CO_2 forcing and its implications for climate sensitivity

H. He *et al.*

Email: haozhe.he@miami.edu

Science **382**, 1051 (2023)
DOI: 10.1126/science.abq6872

The PDF file includes:

Materials and Methods
Figs. S1 to S9
Tables S1 to S6
References

Materials and Methods

Materials

The online double-call $IRF_{4\times CO2}$: The few available online double-call calculations with CO_2 concentrations quadrupled from base-state concentrations, which were requested at low priority by the Cloud Feedbacks Model Intercomparison Project (*53, 54*), are comprehensively used (Tables S1–S3). Note that the currently widely used $IRF_{4\times CO2}$ is twice as large as the $IRF_{2\times CO2}$, as the radiative forcing by CO_2 is a logarithmic function of the atmospheric CO_2 concentration (*28*). These include: six calculations with CMIP6 amip base-states from BCC-CSM2-MR, CanESM5, CNRM-CM6-1, HadGEM3-GC31-LL, INM-CM5-0 and IPSL-CM6A-LR; six calculations with CMIP5 amip base-states from CanAM4, HadGEM2-A, INM-CM4, IPSL-CM5A-LR, IPSL-CM5A-MR and MIROC5; two calculations with CMIP6 1pctCO2 base-states from CNRM-CM6-1 and IPSL-CM6A-LR; a calculation with CMIP6 abrupt-4×CO2 base-state from CNRM-CM6-1; and three calculations with CMIP6 historical base-states from CNRM-CM6-1, IPSL-CM6A-LR and IPSL-CM6A-LR-INCA.

The monthly atmospheric profiles of CMIP model simulations: The monthly atmospheric profiles (including surface temperature, air temperature, and specific humidity) of amip, 1pctCO2, abrupt-4×CO2 and historical period simulations (Tables S1–S3) are used either for the offline double-call IRF calculations or for the analytical IRF calculations. To understand the evolution of upper stratosphere temperature with CO_2 increase and its uncertainty across models, air temperature profiles from the 1pctCO2 simulations are also used.

The atmosphere-only model simulations: The atmosphere-only model simulations forced by boundary conditions of the preindustrial era and recent warming decades along with their corresponding 4×CO2 counterparts [piClim-control / piClim-4×CO2 of Radiative Forcing Model Intercomparison Project (*55*) endorsed by CMIP6 and amip / amip-4×CO2; Table S4] are used to calculate the total infrared RF and to further feed into offline radiation codes for the calculations of the IRF, stratospheric adjustment, and stratospheric adjusted RF. A land-warming correction method (*5*) recommended by Andrews et al. (*56*) is used in the calculation of total infrared RF: The correction method applied in Smith et al. (*12*) assumes that the radiative effect of surface temperature change (i.e., the surface Planck “adjustment”) is the only radiative effect of land warming in fixed-SST experiments.

The simulations for non-linear mechanisms: The simulations, forced by abruptly halving and doubling CO_2 concentration of the preindustrial era [abrupt-0.5×CO2 and abrupt-2×CO2 as part of nonLinMIP (*57*); Table S5], respectively, in addition to the standard abrupt-4×CO2 simulations, are used to explore the state-dependence of CO_2 IRF and stratospheric adjustment as well.

The historical simulations and decomposition simulations: To prove the idea that any forcing agent changes that perturb the upper stratospheric temperature could further impact the climate by modifying the CO_2 radiative forcing, we use historical period simulations from model CanESM5 which has the following simulations available (Table S3): a CMIP6 baseline experiment (historical), historical decomposition simulations from the Detection and Attribution Model Intercomparison Project (*58*), including well-mixed greenhouse-gas-only historical simulations (hist-GHG), anthropogenic-aerosol-only historical simulations (hist-aer), natural-only historical simulations (hist-nat) and total-ozone-only historical simulations (hist-totalO3), and a scenario of the Land Use Model Intercomparison Project (*59*) without land-use change (hist-noLu).

The observations and reanalyses of upper stratospheric temperature: To constrain the IRF spread caused by base-state differences, we adopt 10 hPa air temperature in the year 2020 from satellite observations and three sets of reanalyses, including: Versions 6 & 7 Level 3 AIRS retrievals (*60, 61*), Versions 4 & 5 Level 3 Aura MLS retrievals (*62, 63*), processed level 2A product of SABER Version 2 (*64*), Aqua IR-only, SNPP, and NOAA-20 products produced using the CLIMCAPS algorithm (*65*), ERA5 (*66*), MERRA-2 reanalysis (*67*) and NCEP-DOE Reanalysis 2 (*68*), to diagnose the observational uncertainty.

Methods

The offline double-call $IRF_{4\times CO2}$ calculations: We also estimate $IRF_{4\times CO2}$ using offline radiative transfer models, including a broadband model [SOCRATES (*69, 70*)] and two line-by-line models [ARTS (*71*) and PyRADS (*72*)]. Five sets of configurations are adopted for the SOCRATES offline double-call calculations. The first set of calculations is with a pair of CO_2 concentrations (CO_2 concentration in the year 2000 and correspondingly quadrupled CO_2 concentration) and sigma-level monthly atmospheric profiles in the year 2000 of amip runs for the abovementioned twelve models with online double-call IRFs available. The second set is the same as the previous configuration, except it uses standard 17-pressure-level profiles for all CMIP5/6 models with amip experiments available (Tables S1 and S2). The third set includes three 10-year slice calculations, with three pairs of CO_2 concentrations (CO_2 concentration at years 1–10, 66–75, and 131–140 of 1pctCO2 experiment and correspondingly quadrupled CO_2 concentration) and standard 17-pressure-level atmospheric profiles from the 1pctCO2 experiments for CMIP5/6 models (Tables S1 and S2). With similar configurations as the third set for SOCRATES, line-by-line calculations are also conducted, but instead using three time-mean CO_2 concentrations and atmospheric profiles from the CMIP6 model with the median $IRF_{4\times CO2}$ values in the third set SOCRATES calculations. The fourth configuration is with the pre-industrial and quadrupled CO_2 concentrations as well as standard 17-pressure-level atmospheric profiles from abrupt-4×CO2 experiments for CMIP5/6 models (Tables S1 and S2). The last configuration is with a pair of CO_2 concentrations [time-varying historical CO_2 concentration (*73*) and correspondingly quadrupled CO_2 concentration] and standard pressure-level atmospheric profiles from historical and hist-GHG simulations for CMIP6 models with both simulations (Table S3).

The analytical IRF calculations and decompositions: With an analytical model accounting of the state-dependence of CO_2 IRF (*16*), we also estimate the analytical $IRF_{4\times CO2}$ with base-states from abrupt-4×CO2 experiments for CMIP5/6 models (Tables S1 and S2). The key idea of the analytical model is that the CO_2 IRF can be considered as a swap of surface emission for stratospheric emission. As both the rotational band and continuum of water vapor overlap with the 667 cm^{-1} CO_2 band, water vapor modulates the forcing by replacing surface emission with relative humidity dependent atmospheric emission as follows:

$$\mathcal{F} = 2l \ln\left(\frac{q_f}{q_i}\right)\left[\pi B(\nu_0, \bar{T}_{em}) - \pi B(\nu_0, T_{strat})\right] \quad (1)$$

where l is the 'spectroscopic decay' parameter of 10.2 cm^{-1}, q_i is the initial CO_2 concentration, q_f is the final CO_2 concentration and $\pi B(\nu_0, \bar{T}_{em} \,/\, T_{strat})$ is the hemispherically integrated Planck function at peak absorption wavenumber of CO_2 with either the tropospheric emission temperature or stratospheric emission temperature. Here, $\bar{T}_{em}$ is the tropospheric emission temperature, which is the average of emission temperatures at the low wavenumber (550–600 cm^{-1}) and high wavenumber (750–800 cm^{-1}) sides [see details in Jeevanjee et al. (*16*)]. To better understand the sources of the intermodel IRF spread, a decomposition (piCTL-Tstrat) is also done using the analytical model with stratospheric emission temperature from the original calculations replaced by the counterpart from piControl experiment.

The calculations of the IRF, stratospheric adjustment and stratospheric adjusted RF: To calculate the IRF, stratospheric adjustment and stratospheric adjusted RF, three sets of configurations are adopted for the SOCRATES offline radiation calculations. The first set of calculations is with standard pressure-level profiles of piClim-control and amip simulations of CMIP6 models with piClim-control / piClim-4×CO2 and amip / amip-4×CO2 simulations available (Table S4) and corresponding pre-industrial and recent historical CO_2 concentration, respectively. The second set is the same as the first configuration except it uses correspondingly quadrupled CO_2 concentration, while the third set is the same as the second configuration except the temperature profiles above the dynamical tropopause (*74*) are replaced by the temperature profiles of piClim-4×CO2 and amip-4×CO2 simulations. The difference in radiative fluxes at the TOA from the first and second sets of calculations is the $IRF_{4\times CO2}$. The difference in radiative fluxes from the second and third sets of calculations is the stratospheric adjustment. The stratospheric adjusted RF is the difference in radiative fluxes from the first and third sets of calculations.

The calculations of the IRF and rapid adjustments with radiative kernel method: Following Soden et al. (*75*), the IRF and rapid adjustments (such as the stratospheric adjustment and surface Planck adjustment) are calculated with the HadGEM3 radiative kernels (*76*) for the abovementioned atmosphere-only model simulations as well as the simulations for non-linear mechanisms.

Nonlinear warming contribution: As ozone is the key determining factor for the vertical temperature structure and temperature magnitude at certain altitudes within the stratosphere, we estimate the indirect surface warming effect of ozone depletion in the last 30 years of historical simulations (1985–2014) when stratospheric ozone remained at dangerously low levels and in which stratospheric ozone loss and CO_2 increase coincide. Here, experiments including historical, hist-GHG, hist-aer, hist-nat, hist-totalO3, and hist-noLu from model CanESM5 are used (Table S3). Note that each experiment includes ten ensemble simulations, so the internal variability is excluded from the ensemble-mean results shown in Fig. 4B. The indirect warming effect of the ozone depletion via amplifying CO_2 IRF is primarily included in the difference between ensemble- and time-mean historical surface temperature anomalies and the sum of corresponding anomalies from simulations forced respectively by hist-GHG, hist-aer, hist-nat, and hist-totalO3 as well as the land-use contribution quantified as the difference between historical and hist-noLu, $\Delta T_{\text{nonlinear}} = \Delta T_{\text{historical}} - \Delta T_{\text{hist-GHG}} - \Delta T_{\text{hist-aer}} - \Delta T_{\text{hist-nat}} - \Delta T_{\text{hist-totalO3}} - (\Delta T_{\text{historical}} - \Delta T_{\text{hist-noLu}})$. We should expect trivial or no signal in the nonlinear warming contribution term if there is no indirect effect. We find instead that there is a strong indirect effect, as described in Fig. 4B and the associated text.

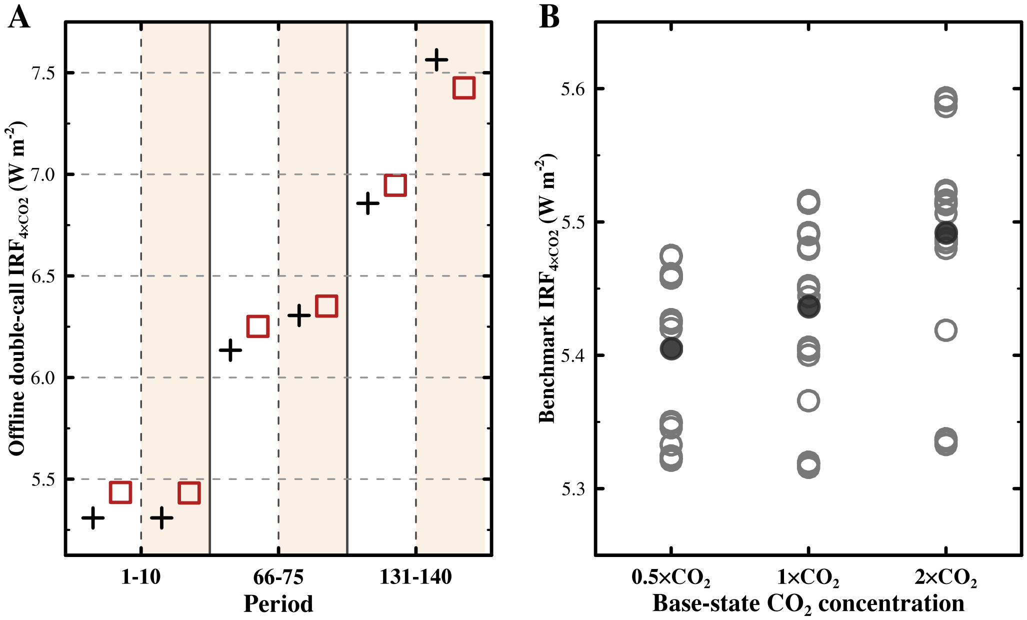

Fig. S1.

(**A**) The line-by-line results (markers with yellow background highlight) shown in Fig. 2A and another set of calculations using identical base-state CO_2 concentration at the preindustrial level for all three periods. The black plus symbols show offline double-call $IRF_{4\times CO2}$ obtained with ARTS, while the red squares show results calculated with PyRADs. The differences between markers without and with yellow background highlights are the base-state CO_2 concentration. The markers without highlight represent the $IRF_{4\times CO2}$ obtained by quadrupling of preindustrial CO_2 concentration, while the highlighted markers show the $IRF_{4\times CO2}$ obtained by quadrupling the varying real-time CO_2 concentration of 1pctCO2 experiment. (**B**) The benchmark line-by-line $IRF_{4\times CO2}$ results of Pincus et al. (*19*), by quadrupling half of the preindustrial CO_2 concentration (0.5×CO2), preindustrial CO_2 concentration (1×CO2), and doubling preindustrial CO_2 concentration (2×CO2), using the same atmospheric profiles. Each open circle in (B) represents the $IRF_{4\times CO2}$ of a line-by-line model, while the solid circle shows the multi-model ensemble mean. The results in (A) show that base-state CO_2 concentration contributes to ~15% $IRF_{4\times CO2}$ increase for the first doubling of base-state CO_2 concentration (period 1–70), while it contributes to ~40% $IRF_{4\times CO2}$ increase for the second doubling of base-state CO_2 concentration (period 71–140). The benchmark $IRF_{4\times CO2}$ results in (B) confirm the small contribution (less than 0.1 W m^{-2}) from base-state CO_2 concentration change to the $IRF_{4\times CO2}$ increase for the first doubling of base-state CO_2 concentration.

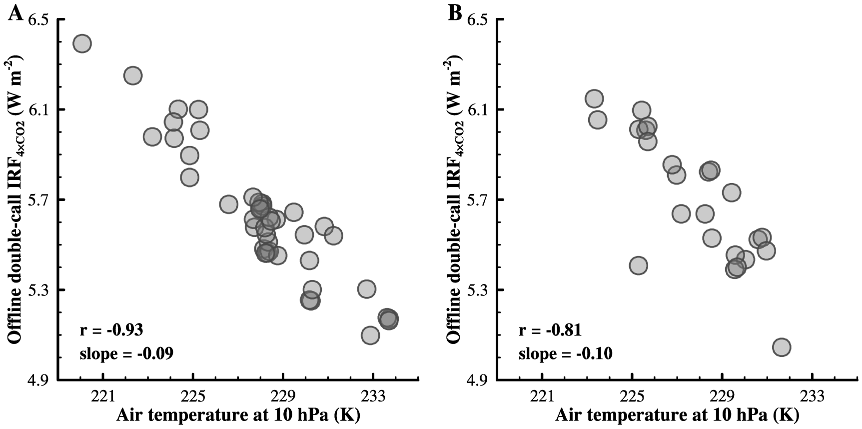

Fig. S2.

Scatterplots of global- and annual-mean air temperature at 10 hPa of each model in the year 2000 of the amip experiment versus its corresponding offline double-call IRF$_{4\times CO2}$ for (**A**) CMIP6 and (**B**) CMIP5 models.

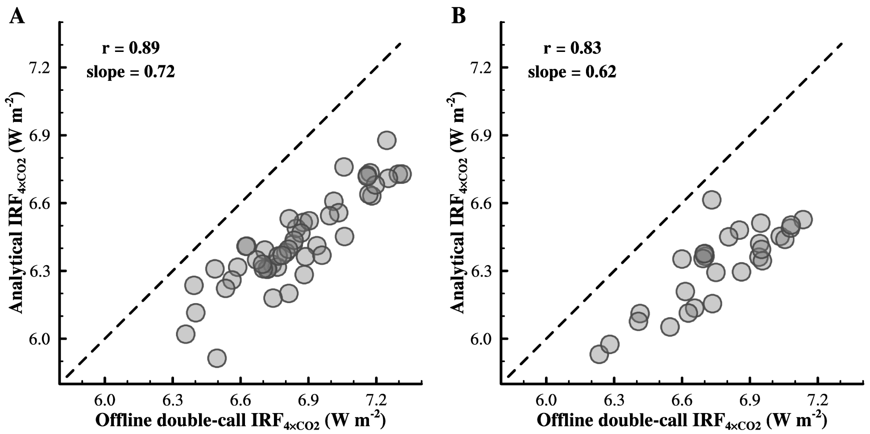

Fig. S3.

Comparisons of the global- and time-mean IRF$_{4\times\mathrm{CO2}}$ in years 121–140 from the offline double-call and analytical model calculations for (**A**) CMIP6 and (**B**) CMIP5 models. The correlation between global- and time-mean IRF$_{4\times\mathrm{CO2}}$ in every 10 of 150-year experiments from the offline double-call and analytical model calculations has a range from 0.88 (0.82) to 0.89 (0.83) for CMIP6 (CMIP5) models.

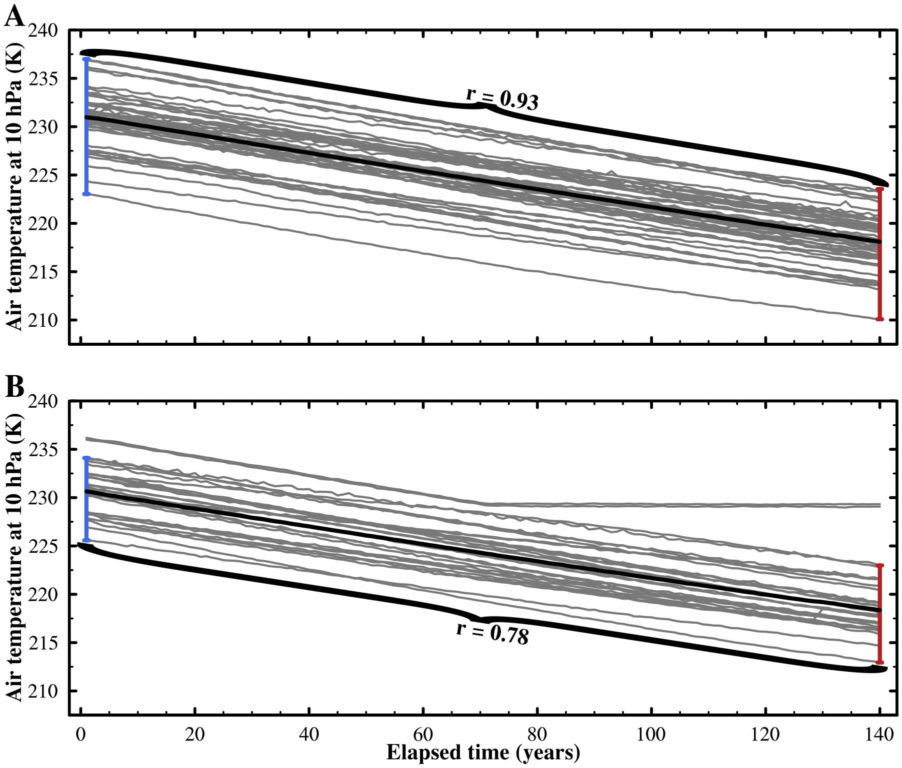

Fig. S4.

Time series of global- and annual-mean 10 hPa air temperature under 1pctCO2 scenario from (**A**) CMIP6 and (**B**) CMIP5 models. Each gray line in (A) and (B) represents the 10 hPa temperature evolution of a model, while the thick black line shows the multi-model ensemble mean. The curly brackets in (A) and (B) highlight the correlation between 10 hPa air temperature at years 1 and 140. Note that the temperature of two CMIP5 models (GFDL-ESM2G and GFDL-ESM2M) is excluded from the correlation calculations, since their CO_2 concentration increases end at year 70.

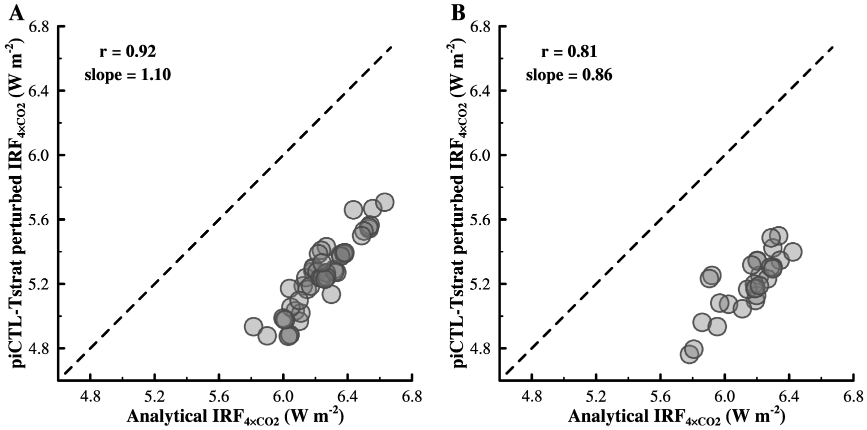

Fig. S5.

Comparisons of the global- and time-mean original analytical $\mathrm{IRF}_{4\times\mathrm{CO2}}$ in years 2–11 and that obtained with stratospheric emission temperature from piControl runs (piCTL-Tstrat) for (**A**) CMIP6 and (**B**) CMIP5 models. The correlation between global- and time-mean original analytical $\mathrm{IRF}_{4\times\mathrm{CO2}}$ in every 10 of 150-year experiments and that obtained with the piCTL-Tstrat perturbed calculations has a range from 0.90 (0.81) to 0.92 (0.86) for the CMIP6 (CMIP5) models.

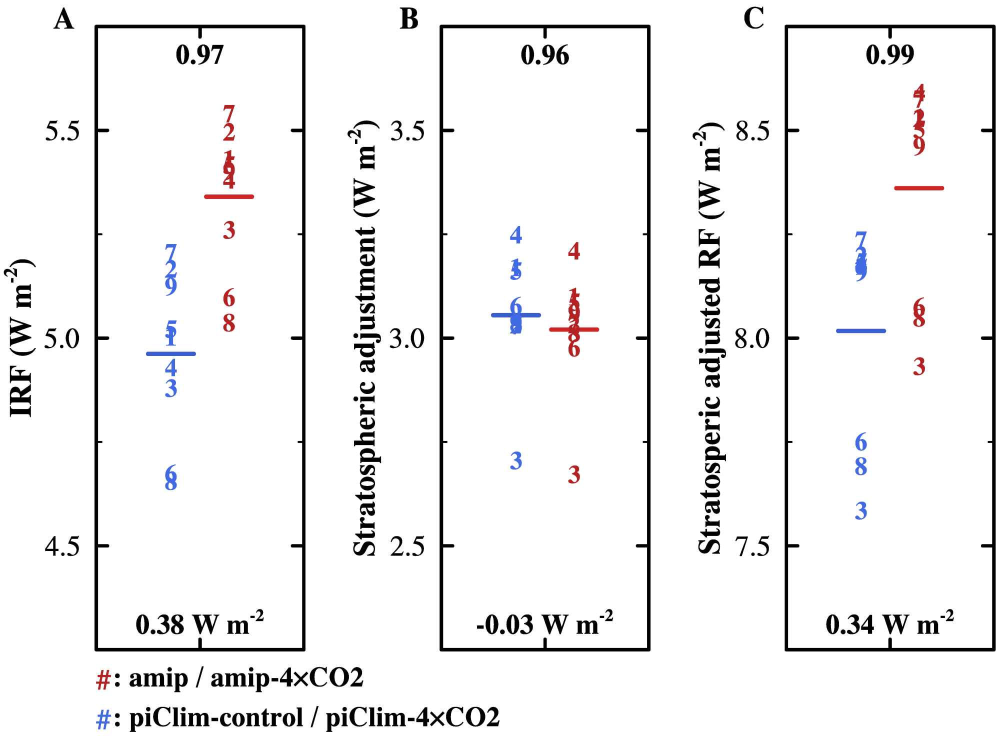

Fig. S6.

Comparisons of the (**A**) IRF, (**B**) stratospheric adjustment, and (**C**) stratospheric adjusted RF calculated based on piClim-control / piClim-4×CO2 and amip / amip-4×CO2 simulations, respectively, for those CMIP6 models with all these simulations available. Numbered markers correspond to the CMIP6 models listed in Table S4. Numbers at the top of each plot give the correlation coefficient between estimates from piClim-control / piClim-4×CO2 and amip / amip-4×CO2 simulations, while the numbers at the bottom provide the difference in the corresponding multi-model ensemble mean. The results are obtained by three sets of radiative transfer calculations with the SOCRATES. The first set of calculations is with standard pressure-level profiles of piClim-control and amip simulations as well as corresponding pre-industrial and recent historical CO_2 concentrations, respectively. The second set is the same as the first configuration except it uses correspondingly quadrupled CO_2 concentrations, while the third set is the same as the second configuration except the temperature profiles above the dynamical tropopause (*74*) are replaced by the temperature profiles of piClim-4×CO2 and amip-4×CO2 simulations. Here, the $IRF_{4\times CO2}$ is the difference in radiative fluxes at the TOA from the first and second sets of calculations, while the stratospheric adjustment is the difference in radiative fluxes from the second and third sets of calculations. The stratospheric adjusted RF is the difference in radiative fluxes from the first and third sets of calculations.

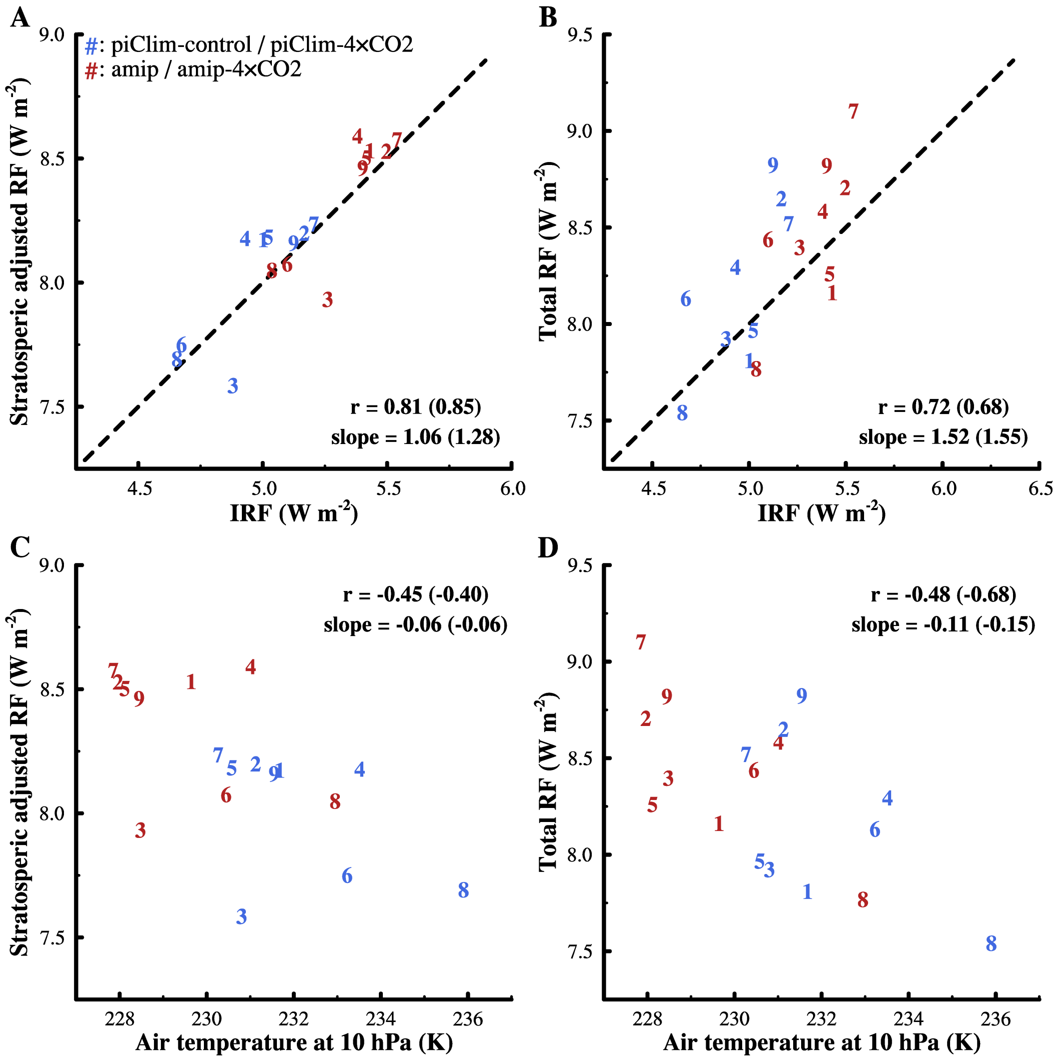

Fig. S7.

Scatterplots of (**A**) stratospheric adjusted RF and (**B**) total RF versus IRF for CMIP6 models with piClim-control / piClim-4×CO2 and amip / amip-4×CO2 simulations available. Numbered markers correspond to the CMIP6 models listed in Table S4. Scatterplots (**C**) and (**D**) are the same as (**A**) and (**B**), except for comparing to air temperature at 10 hPa instead of the IRF. The values in front of (in) parentheses are values calculated with piClim-control / piClim-4×CO2 (amip / amip-4×CO2) simulations. Here, the IRF and stratospheric adjusted RF are the same as the results shown in Fig. S6. The total RF is referring to the total infrared RF, which is quantified as the difference in the outgoing longwave radiation between piClim-control and piClim-4×CO2 simulations as well as amip and amip-4×CO2 simulations. A land-warming correction method (*5*) recommended by Andrews et al. (*56*) is used in the calculation of total infrared RF: The correction method applied in Smith et al. (*12*) assumes that the radiative effect of surface temperature change (i.e., the surface Planck "adjustment") is the only radiative effect of land warming in fixed-SST experiments.

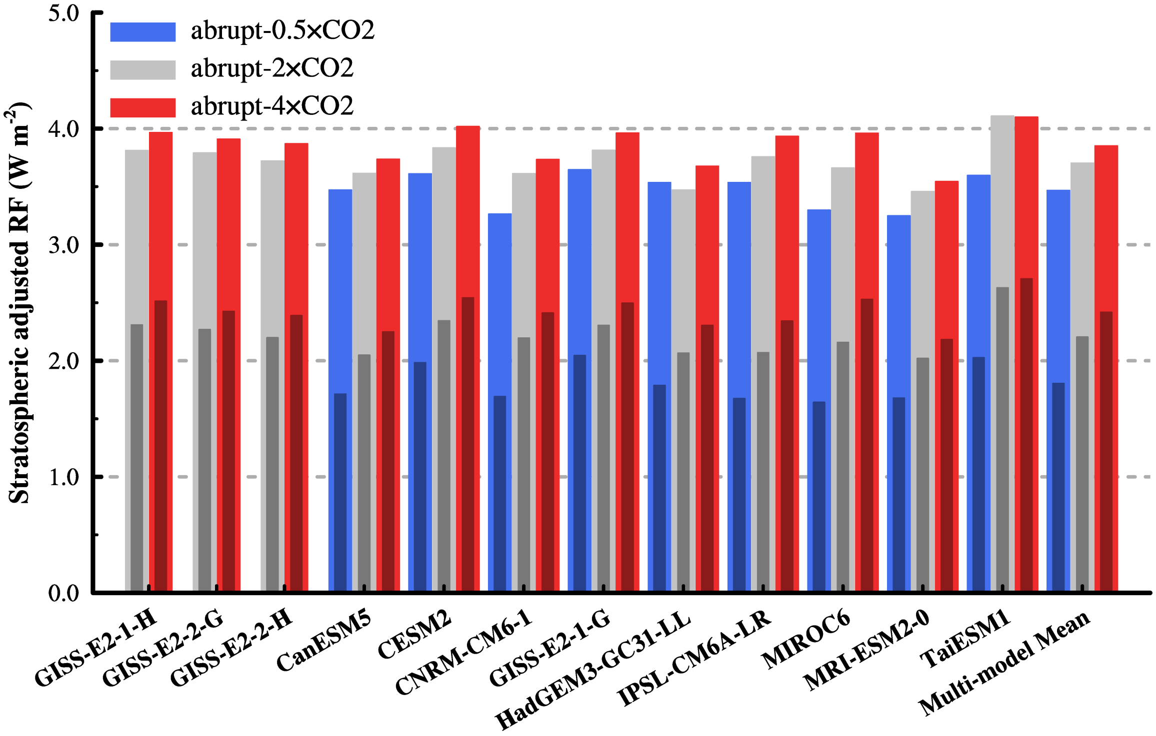

Fig. S8.

Comparison of stratospheric adjusted RF per CO_2 doubling for abrupt-0.5×CO2, abrupt-2×CO2, and abrupt-4×CO2 simulations. The overlaid thin and dark bars represent the corresponding IRF per CO_2 doubling. Note that models GISS-E2-1-H, GISS-E2-2-G, and GISS-E2-2-H are excluded from the multi-model mean analysis, which is the bars at the far right, since the abrupt-0.5×CO2 simulations of these models are not available. Following Soden et al. (*75*), the IRF and stratospheric adjustment are calculated with the HadGEM3 radiative kernels (*76*). Note that the IRF is the value of the first year within the whole 150-year coupled simulations, in order to exclude the IRF increase due to the surface warming in the following simulations. The stratospheric temperature adjustment is the average value of the whole 150-year coupled simulations, since the stratospheric temperature equilibrates in almost the first year and remains the same for the entire 150-year coupled simulations. The stratospheric adjusted RF is the sum of the IRF and stratospheric adjustment.

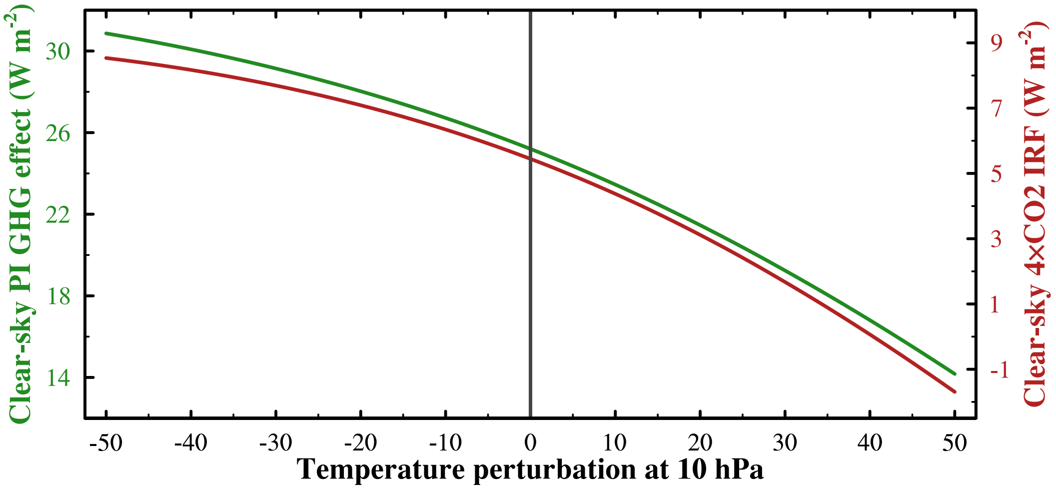

Fig. S9.

Sensitivities of the preindustrial CO_2 greenhouse effect (climatological CO_2 IRF) and $IRF_{4\times CO2}$ to the temperature perturbation at 10 hPa. The results are obtained by a set of radiative transfer calculations with SOCRATES. The calculations use the monthly climatology of piControl tropospheric profiles [including temperature and humidity from surface to the dynamical tropopause (*74*)] as well as the monthly climatological stratospheric humidity. The stratospheric temperature profiles used in the calculations are reconstructed via logarithmic interpolation with monthly climatological tropopause temperature and perturbed air temperature at 10 hPa. The perturbed air temperature at 10 hPa is the sum of monthly climatological 10 hPa temperature and every 1 K perturbation ranging from -50 to 50 K. The preindustrial CO_2 greenhouse effect is the radiative flux difference between radiative transfer calculations with and without the preindustrial CO_2, while the $IRF_{4\times CO2}$ is the difference between calculations with the preindustrial CO_2 and corresponding quadrupling CO_2 concentrations.

Table S1.

A list of the CMIP6 climate models analyzed in this study. Simulations with online double-call available for the models are highlighted in bold.

	Institution	Model	DOI amip	DOI piControl	DOI 1pctCO2	DOI abrupt-4×CO2
1	CSIRO-ARCCSS	ACCESS-CM2	doi:10.22033/ESGF/CMIP6.4239	doi:10.22033/ESGF/CMIP6.4311	doi:10.22033/ESGF/CMIP6.4230	doi:10.22033/ESGF/CMIP6.4237
2	CSIRO	ACCESS-ESM1-5	doi:10.22033/ESGF/CMIP6.4240	doi:10.22033/ESGF/CMIP6.4312	doi:10.22033/ESGF/CMIP6.4231	doi:10.22033/ESGF/CMIP6.4238
3	AWI	AWI-CM-1-1-MR		doi:10.22033/ESGF/CMIP6.2777	doi:10.22033/ESGF/CMIP6.2543	doi:10.22033/ESGF/CMIP6.2568
4	BCC	BCC-CSM2-MR	**doi:10.22033/ESGF/CMIP6.2850**	doi:10.22033/ESGF/CMIP6.3016	doi:10.22033/ESGF/CMIP6.2833	doi:10.22033/ESGF/CMIP6.2845
5	BCC	BCC-ESM1	doi:10.22033/ESGF/CMIP6.2851	doi:10.22033/ESGF/CMIP6.3017	doi:10.22033/ESGF/CMIP6.2834	doi:10.22033/ESGF/CMIP6.2846
6	CCCma	CanESM5	**doi:10.22033/ESGF/CMIP6.3535**	doi:10.22033/ESGF/CMIP6.3673	doi:10.22033/ESGF/CMIP6.3151	doi:10.22033/ESGF/CMIP6.3532
7	CAS	CAS-ESM2-0	doi:10.22033/ESGF/CMIP6.3180	doi:10.22033/ESGF/CMIP6.3445	doi:10.22033/ESGF/CMIP6.3052	doi:10.22033/ESGF/CMIP6.3174
8	NCAR	CESM2	doi:10.22033/ESGF/CMIP6.7522	doi:10.22033/ESGF/CMIP6.7733	doi:10.22033/ESGF/CMIP6.7497	doi:10.22033/ESGF/CMIP6.7519
9	NCAR	CESM2-FV2	doi:10.22033/ESGF/CMIP6.11287	doi:10.22033/ESGF/CMIP6.11301	doi:10.22033/ESGF/CMIP6.11283	doi:10.22033/ESGF/CMIP6.11285
10	NCAR	CESM2-WACCM	doi:10.22033/ESGF/CMIP6.10041	doi:10.22033/ESGF/CMIP6.10094	doi:10.22033/ESGF/CMIP6.10028	doi:10.22033/ESGF/CMIP6.10039
11	NCAR	CESM2-WACCM-FV2	doi:10.22033/ESGF/CMIP6.11288	doi:10.22033/ESGF/CMIP6.11302	doi:10.22033/ESGF/CMIP6.11284	doi:10.22033/ESGF/CMIP6.11286
12	THU	CIESM	doi:10.22033/ESGF/CMIP6.8810	doi:10.22033/ESGF/CMIP6.8849	doi:10.22033/ESGF/CMIP6.8801	doi:10.22033/ESGF/CMIP6.8807
13	CMCC	CMCC-CM2-SR5	doi:10.22033/ESGF/CMIP6.3737	doi:10.22033/ESGF/CMIP6.3874	doi:10.22033/ESGF/CMIP6.3721	doi:10.22033/ESGF/CMIP6.3731
14	CMCC	CMCC-ESM2		doi:10.22033/ESGF/CMIP6.13241	doi:10.22033/ESGF/CMIP6.13169	doi:10.22033/ESGF/CMIP6.13174
15	CNRM-CERFACS	CNRM-CM6-1	**doi:10.22033/ESGF/CMIP6.3922**	doi:10.22033/ESGF/CMIP6.4163	**doi:10.22033/ESGF/CMIP6.3712**	**doi:10.22033/ESGF/CMIP6.3916**
16	CNRM-CERFACS	CNRM-CM6-1-HR	doi:10.22033/ESGF/CMIP6.3923	doi:10.22033/ESGF/CMIP6.4164	doi:10.22033/ESGF/CMIP6.3713	doi:10.22033/ESGF/CMIP6.3917
17	DOE	E3SM-1-0	doi:10.22033/ESGF/CMIP6.4492	doi:10.22033/ESGF/CMIP6.4499	doi:10.22033/ESGF/CMIP6.4490	doi:10.22033/ESGF/CMIP6.4491
18	EC-Earth-Consortium	EC-Earth3	doi:10.22033/ESGF/CMIP6.4529	doi:10.22033/ESGF/CMIP6.4842	doi:10.22033/ESGF/CMIP6.4501	doi:10.22033/ESGF/CMIP6.4518
19	EC-Earth-Consortium	EC-Earth3-AerChem	doi:10.22033/ESGF/CMIP6.4530	doi:10.22033/ESGF/CMIP6.4843	doi:10.22033/ESGF/CMIP6.4502	doi:10.22033/ESGF/CMIP6.4519
20	EC-Earth-Consortium	EC-Earth3-CC	doi:10.22033/ESGF/CMIP6.4531	doi:10.22033/ESGF/CMIP6.4844	doi:10.22033/ESGF/CMIP6.4503	doi:10.22033/ESGF/CMIP6.4520
21	EC-Earth-Consortium	EC-Earth3-Veg	doi:10.22033/ESGF/CMIP6.4535	doi:10.22033/ESGF/CMIP6.4848	doi:10.22033/ESGF/CMIP6.4507	doi:10.22033/ESGF/CMIP6.4524
22	CAS	FGOALS-f3-L	doi:10.22033/ESGF/CMIP6.3182	doi:10.22033/ESGF/CMIP6.3447	doi:10.22033/ESGF/CMIP6.3054	doi:10.22033/ESGF/CMIP6.3176
23	CAS	FGOALS-g3	doi:10.22033/ESGF/CMIP6.3183	doi:10.22033/ESGF/CMIP6.3448	doi:10.22033/ESGF/CMIP6.3055	doi:10.22033/ESGF/CMIP6.3177
24	NOAA-GFDL	GFDL-CM4	doi:10.22033/ESGF/CMIP6.8494	doi:10.22033/ESGF/CMIP6.8666	doi:10.22033/ESGF/CMIP6.8470	doi:10.22033/ESGF/CMIP6.8486
25	NOAA-GFDL	GFDL-ESM4	doi:10.22033/ESGF/CMIP6.8497	doi:10.22033/ESGF/CMIP6.8669	doi:10.22033/ESGF/CMIP6.8473	doi:10.22033/ESGF/CMIP6.8489
26	NASA-GISS	GISS-E2-1-G	doi:10.22033/ESGF/CMIP6.6984	doi:10.22033/ESGF/CMIP6.7380	doi:10.22033/ESGF/CMIP6.6950	doi:10.22033/ESGF/CMIP6.6976
27	NASA-GISS	GISS-E2-1-H		doi:10.22033/ESGF/CMIP6.7381	doi:10.22033/ESGF/CMIP6.6951	doi:10.22033/ESGF/CMIP6.6977
28	NASA-GISS	GISS-E2-2-G	doi:10.22033/ESGF/CMIP6.6986	doi:10.22033/ESGF/CMIP6.7382	doi:10.22033/ESGF/CMIP6.6952	doi:10.22033/ESGF/CMIP6.6978
29	NASA-GISS	GISS-E2-2-H		doi:10.22033/ESGF/CMIP6.15874	doi:10.22033/ESGF/CMIP6.15864	doi:10.22033/ESGF/CMIP6.15865
30	MOHC	HadGEM3-GC31-LL	**doi:10.22033/ESGF/CMIP6.5853**	doi:10.22033/ESGF/CMIP6.6294	doi:10.22033/ESGF/CMIP6.5788	doi:10.22033/ESGF/CMIP6.5839
31	MOHC	HadGEM3-GC31-MM	doi:10.22033/ESGF/CMIP6.5856	doi:10.22033/ESGF/CMIP6.6297	doi:10.22033/ESGF/CMIP6.5791	doi:10.22033/ESGF/CMIP6.5842
32	MPI-M	ICON-ESM-LR		doi:10.22033/ESGF/CMIP6.6673	doi:10.22033/ESGF/CMIP6.6433	doi:10.22033/ESGF/CMIP6.6457
33	INM	INM-CM4-8	doi:10.22033/ESGF/CMIP6.4934	doi:10.22033/ESGF/CMIP6.5080	doi:10.22033/ESGF/CMIP6.4928	doi:10.22033/ESGF/CMIP6.4931
34	INM	INM-CM5-0	**doi:10.22033/ESGF/CMIP6.4935**	doi:10.22033/ESGF/CMIP6.5081	doi:10.22033/ESGF/CMIP6.4929	doi:10.22033/ESGF/CMIP6.4932
35	IPSL	IPSL-CM5A2-INCA		doi:10.22033/ESGF/CMIP6.13683	doi:10.22033/ESGF/CMIP6.13642	doi:10.22033/ESGF/CMIP6.13644
36	IPSL	IPSL-CM6A-LR	**doi:10.22033/ESGF/CMIP6.5113**	doi:10.22033/ESGF/CMIP6.5251	**doi:10.22033/ESGF/CMIP6.5049**	doi:10.22033/ESGF/CMIP6.5109
37	NIMS-KMA	KACE-1-0-G	doi:10.22033/ESGF/CMIP6.8350	doi:10.22033/ESGF/CMIP6.8425	doi:10.22033/ESGF/CMIP6.8333	doi:10.22033/ESGF/CMIP6.8348
38	KIOST	KIOST-ESM	doi:10.22033/ESGF/CMIP6.5289	doi:10.22033/ESGF/CMIP6.5303	doi:10.22033/ESGF/CMIP6.5283	doi:10.22033/ESGF/CMIP6.5288
39	MIROC	MIROC6	doi:10.22033/ESGF/CMIP6.5422	doi:10.22033/ESGF/CMIP6.5711	doi:10.22033/ESGF/CMIP6.5371	doi:10.22033/ESGF/CMIP6.5411
40	MIROC	MIROC-ES2L	doi:10.22033/ESGF/CMIP6.5421	doi:10.22033/ESGF/CMIP6.5710	doi:10.22033/ESGF/CMIP6.5370	doi:10.22033/ESGF/CMIP6.5410
41	HAMMOZ-Consortium	MPI-ESM-1-2-HAM	doi:10.22033/ESGF/CMIP6.5001	doi:10.22033/ESGF/CMIP6.5037	doi:10.22033/ESGF/CMIP6.4999	doi:10.22033/ESGF/CMIP6.5000
42	MPI-M	MPI-ESM1-2-HR	doi:10.22033/ESGF/CMIP6.6463	doi:10.22033/ESGF/CMIP6.6674	doi:10.22033/ESGF/CMIP6.6434	doi:10.22033/ESGF/CMIP6.6458
43	MPI-M	MPI-ESM1-2-LR	doi:10.22033/ESGF/CMIP6.6464	doi:10.22033/ESGF/CMIP6.6675	doi:10.22033/ESGF/CMIP6.6435	doi:10.22033/ESGF/CMIP6.6459
44	MRI	MRI-ESM2-0	doi:10.22033/ESGF/CMIP6.6758	doi:10.22033/ESGF/CMIP6.6900	doi:10.22033/ESGF/CMIP6.5356	doi:10.22033/ESGF/CMIP6.6755
45	NUIST	NESM3	doi:10.22033/ESGF/CMIP6.8720	doi:10.22033/ESGF/CMIP6.8776	doi:10.22033/ESGF/CMIP6.8709	doi:10.22033/ESGF/CMIP6.8719
46	NCC	NorCPM1	doi:10.22033/ESGF/CMIP6.10863	doi:10.22033/ESGF/CMIP6.10896	doi:10.22033/ESGF/CMIP6.10861	doi:10.22033/ESGF/CMIP6.10862
47	NCC	NorESM2-LM	doi:10.22033/ESGF/CMIP6.7848	doi:10.22033/ESGF/CMIP6.8217	doi:10.22033/ESGF/CMIP6.7802	doi:10.22033/ESGF/CMIP6.7836
48	NCC	NorESM2-MM	doi:10.22033/ESGF/CMIP6.7852	doi:10.22033/ESGF/CMIP6.8221	doi:10.22033/ESGF/CMIP6.7806	doi:10.22033/ESGF/CMIP6.7840
49	SNU	SAM0-UNICON	doi:10.22033/ESGF/CMIP6.7784	doi:10.22033/ESGF/CMIP6.7791	doi:10.22033/ESGF/CMIP6.7782	doi:10.22033/ESGF/CMIP6.7783
50	AS-RCEC	TaiESM1	doi:10.22033/ESGF/CMIP6.9713	doi:10.22033/ESGF/CMIP6.9798	doi:10.22033/ESGF/CMIP6.9702	doi:10.22033/ESGF/CMIP6.9709
51	MOHC	UKESM1-0-LL	doi:10.22033/ESGF/CMIP6.5857	doi:10.22033/ESGF/CMIP6.6298	doi:10.22033/ESGF/CMIP6.5792	doi:10.22033/ESGF/CMIP6.5843

Table S2.

A list of the CMIP5 climate models analyzed in this study. Simulations with online double-call available for the models are highlighted in bold.

	Institution	Model	amip	piControl	1pctCO2	abrupt4×CO2
1	CSIRO-BOM	ACCESS1-0	O	O	O	O
2	CSIRO-BOM	ACCESS1-3	O	O	O	O
3	BCC	bcc-csm1-1	O	O	O	O
4	BCC	bcc-csm1-1-m	O	O	O	O
5	BNU	BNU-ESM	O	O	O	O
6	CCCma	CanESM2 / CanAM4	**O**	O	O	O
7	NCAR	CCSM4	O	O	O	O
8	CNRM-CERFACS	CNRM-CM5	O	O	O	O
9	CNRM-CERFACS	CNRM-CM5-2		O	O	O
10	CSIRO-QCCCE	CSIRO-Mk3-6-0	O	O	O	O
11	LASG-CESS	FGOALS-g2	O	O	O	O
12	LASG-IAP	FGOALS-s2	O	O	O	O
13	NOAA-GFDL	GFDL-CM3	O	O	O	O
14	NOAA-GFDL	GFDL-ESM2G		O	O	O
15	NOAA-GFDL	GFDL-ESM2M		O	O	O
16	NASA-GISS	GISS-E2-H		O	O	O
17	NASA-GISS	GISS-E2-R	O	O	O	O
18	MOHC	HadGEM2-ES / HadGEM2-A	**O**	O	O	O
19	INM	INM-CM4	**O**	O	O	O
20	IPSL	IPSL-CM5A-LR	**O**	O	O	O
21	IPSL	IPSL-CM5A-MR	**O**	O	O	O
22	IPSL	IPSL-CM5B-LR	O	O	O	O
23	MIROC	MIROC5	**O**	O	O	O
24	MIROC	MIROC-ESM	O	O	O	O
25	MPI-M	MPI-ESM-LR	O	O	O	O
26	MPI-M	MPI-ESM-MR	O	O	O	O
27	MPI-M	MPI-ESM-P		O	O	O
28	MRI	MRI-CGCM3	O	O	O	O
29	NCC	NorESM1-M	O	O	O	O

Table S3.

A list of historical period simulations of the CMIP6 climate models analyzed in this study. Simulations with online double-call available for the models are highlighted in bold.

	Institution	Model	DOI historical	DOI hist-GHG	DOI hist-aer	DOI hist-nat	DOI hist-totalO3	DOI hist-noLu
1	CSIRO-ARCCSS	ACCESS-CM2	doi:10.22033/ESGF/CMIP6.4271	doi:10.22033/ESGF/CMIP6.14365				
2	CSIRO	ACCESS-ESM1-5	doi:10.22033/ESGF/CMIP6.4272	doi:10.22033/ESGF/CMIP6.1436				
3	CCCma	CanESM5	doi:10.22033/ESGF/CMIP6.3610	doi:10.22033/ESGF/CMIP6.3596	doi:10.22033/ESGF/CMIP6.3597	doi:10.22033/ESGF/CMIP6.3601	doi:10.22033/ESGF/CMIP6.12405	doi:10.22033/ESGF/CMIP6.3602
4	NCAR	CESM2	doi:10.22033/ESGF/CMIP6.7627	doi:10.22033/ESGF/CMIP6.7604				
5	CNRM-CERFACS	CNRM-CM6-1	**doi:10.22033/ESGF/CMIP6.4066**	doi:10.22033/ESGF/CMIP6.4043				
6	DOE	E3SM-1-0	doi:10.22033/ESGF/CMIP6.4497	O				
7	NASA-GISS	GISS-E2-1-G	doi:10.22033/ESGF/CMIP6.7127	doi:10.22033/ESGF/CMIP6.7079				
8	NOAA-GFDL	GFDL-ESM4	doi:10.22033/ESGF/CMIP6.8597	doi:10.22033/ESGF/CMIP6.8570				
9	MOHC	HadGEM3-GC31-LL	doi:10.22033/ESGF/CMIP6.6109	doi:10.22033/ESGF/CMIP6.6051				
10	IPSL	IPSL-CM6A-LR	**doi:10.22033/ESGF/CMIP6.5195**	doi:10.22033/ESGF/CMIP6.13825				
11	IPSL	IPSL-CM6A-LR-INCA	**doi:10.22033/ESGF/CMIP6.13601**					
12	MIROC	MIROC6	doi:10.22033/ESGF/CMIP6.5603	doi:10.22033/ESGF/CMIP6.5578				
13	MRI	MRI-ESM2-0	doi:10.22033/ESGF/CMIP6.6842	doi:10.22033/ESGF/CMIP6.6820				
14	NCC	NorESM2-LM	doi:10.22033/ESGF/CMIP6.8036	doi:10.22033/ESGF/CMIP6.7966				

Table S4.

A list of AMIP simulations of the CMIP6 climate models analyzed in this study, to help to understand the state-dependence of both the IRF and rapid adjustments.

	Institution	Model	DOI piClim-control	DOI piClim-4×CO2	DOI amip	DOI amip-4×CO2
1	CCCma	CanESM5	doi:10.22033/ESGF/CMIP6.3662	doi:10.22033/ESGF/CMIP6.3659	doi:10.22033/ESGF/CMIP6.3535	doi:10.22033/ESGF/CMIP6.3536
2	NCAR	CESM2	doi:10.22033/ESGF/CMIP6.7721	doi:10.22033/ESGF/CMIP6.7706	doi:10.22033/ESGF/CMIP6.7522	doi:10.22033/ESGF/CMIP6.7523
3	CNRM-CERFACS	CNRM-CM6-1	doi:10.22033/ESGF/CMIP6.4151	doi:10.22033/ESGF/CMIP6.4136	doi:10.22033/ESGF/CMIP6.3922	doi:10.22033/ESGF/CMIP6.3926
4	NOAA-GFDL	GFDL-CM4	doi:10.22033/ESGF/CMIP6.8653	doi:10.22033/ESGF/CMIP6.8638	doi:10.22033/ESGF/CMIP6.8494	doi:10.22033/ESGF/CMIP6.8499
5	MOHC	HadGEM3-GC31-LL	doi:10.22033/ESGF/CMIP6.6275	doi:10.22033/ESGF/CMIP6.6224	doi:10.22033/ESGF/CMIP6.5853	doi:10.22033/ESGF/CMIP6.5861
6	IPSL	IPSL-CM6A-LR	doi:10.22033/ESGF/CMIP6.5239	doi:10.22033/ESGF/CMIP6.5236	doi:10.22033/ESGF/CMIP6.5113	doi:10.22033/ESGF/CMIP6.5114
7	MIROC	MIROC6	doi:10.22033/ESGF/CMIP6.5697	doi:10.22033/ESGF/CMIP6.5682	doi:10.22033/ESGF/CMIP6.5422	doi:10.22033/ESGF/CMIP6.5427
8	MRI	MRI-ESM2-0	doi:10.22033/ESGF/CMIP6.6888	doi:10.22033/ESGF/CMIP6.6873	doi:10.22033/ESGF/CMIP6.6758	doi:10.22033/ESGF/CMIP6.6759
9	NCC	NorESM2-LM	doi:10.22033/ESGF/CMIP6.8179	doi:10.22033/ESGF/CMIP6.8122	doi:10.22033/ESGF/CMIP6.7848	O

Table S5.

A list of simulations for non-linear mechanisms of the CMIP6 climate models analyzed in this study, to help to understand the state-dependence of both the IRF and stratospheric adjustment.

	Institution	Model	DOI abrupt-0p5×CO2	DOI abrupt-2×CO2	DOI abrupt-4×CO2
1	CCCma	CanESM5	doi:10.22033/ESGF/CMIP6.3530	doi:10.22033/ESGF/CMIP6.3531	doi:10.22033/ESGF/CMIP6.3532
2	NCAR	CESM2	doi:10.22033/ESGF/CMIP6.7517	doi:10.22033/ESGF/CMIP6.7518	doi:10.22033/ESGF/CMIP6.7519
3	CNRM-CERFACS	CNRM-CM6-1	doi:10.22033/ESGF/CMIP6.3914	doi:10.22033/ESGF/CMIP6.3915	doi:10.22033/ESGF/CMIP6.3916
4	NASA-GISS	GISS-E2-1-G	doi:10.22033/ESGF/CMIP6.6972	doi:10.22033/ESGF/CMIP6.6974	doi:10.22033/ESGF/CMIP6.6976
5	NASA-GISS	GISS-E2-1-H		doi:10.22033/ESGF/CMIP6.13965	doi:10.22033/ESGF/CMIP6.6977
6	NASA-GISS	GISS-E2-2-G		doi:10.22033/ESGF/CMIP6.11688	doi:10.22033/ESGF/CMIP6.6978
7	NASA-GISS	GISS-E2-2-H		O	doi:10.22033/ESGF/CMIP6.15865
8	MOHC	HadGEM3-GC31-LL	doi:10.22033/ESGF/CMIP6.5833	doi:10.22033/ESGF/CMIP6.5834	doi:10.22033/ESGF/CMIP6.5839
9	IPSL	IPSL-CM6A-LR	doi:10.22033/ESGF/CMIP6.5106	doi:10.22033/ESGF/CMIP6.5107	doi:10.22033/ESGF/CMIP6.5109
10	MIROC	MIROC6	doi:10.22033/ESGF/CMIP6.5405	doi:10.22033/ESGF/CMIP6.5407	doi:10.22033/ESGF/CMIP6.5411
11	MRI	MRI-ESM2-0	doi:10.22033/ESGF/CMIP6.6753	doi:10.22033/ESGF/CMIP6.6754	doi:10.22033/ESGF/CMIP6.6755
12	AS-RCEC	TaiESM1	doi:10.22033/ESGF/CMIP6.9706	doi:10.22033/ESGF/CMIP6.9707	doi:10.22033/ESGF/CMIP6.9709

Table S6.

A list of global- and annual-mean values of the 10 hPa air temperature (T10) in the year 2020 from multiple sets of observations and reanalyses.

Dataset	**AIRS**		**MLS**		**SABER**	**CLIMCAPS**			**ERA5**	**MERRA2**	**NCEP2**
(Version)	*V6*	*V7*	*V4*	*V5*		*Aqua*	*SNPP*	*NOAA-20*			
T10 (K)	227.7	227.2	226.6	226.6	228.4	227.7	227.8	227.7	228.3	227.2	227.5

References and Notes

1. G. Myhre, D. Shindell, F.-M. Bréon, W. Collins, J. Fuglestvedt, J. Huang, D. Koch, J.-F. Lamarque, D. Lee, B. Mendoza, T. Nakajima, A. Robock, G. Stephens, T. Takemura, H. Zhang, “Anthropogenic and natural radiative forcing,” in *Climate Change 2013 - The Physical Science Basis. Contribution of Working Group I to the Fifth Assessment Report of the Intergovernmental Panel on Climate Change* (Cambridge Univ. Press, 2009), pp. 659–740.

2. R. J. Kramer, H. He, B. J. Soden, L. Oreopoulos, G. Myhre, P. M. Forster, C. J. Smith, Observational evidence of increasing global radiative forcing. *Geophys. Res. Lett.* **48**, e2020GL091585 (2021). doi:10.1029/2020GL091585

3. O. Boucher, D. Randall, P. Artaxo, C. Bretherton, G. Feingold, P. Forster, V.-M. Kerminen, Y. Kondo, H. Liao, U. Lohmann, P. Rasch, S. K. Satheesh, S. Sherwood, B. Stevens, X. Y. Zhang, “Clouds and aerosols,” in *Climate Change 2013 - The Physical Science Basis. Contribution of Working Group I to the Fifth Assessment Report of the Intergovernmental Panel on Climate Change* (Cambridge Univ. Press, 2009), pp. 571–657.

4. S. C. Sherwood, S. Bony, O. Boucher, C. Bretherton, P. M. Forster, J. M. Gregory, B. Stevens, Adjustments in the forcing-feedback framework for understanding climate change. *Bull. Am. Meteorol. Soc.* **96**, 217–228 (2015). doi:10.1175/BAMS-D-13-00167.1

5. P. M. Forster, T. Richardson, A. C. Maycock, C. J. Smith, B. H. Samset, G. Myhre, T. Andrews, R. Pincus, M. Schulz, Recommendations for diagnosing effective radiative forcing from climate models for CMIP6. *J. Geophys. Res. Atmos.* **121**, 12,460–12,475 (2016). doi:10.1002/2016JD025320

6. V. Ramaswamy, W. Collins, J. Haywood, J. Lean, N. Mahowald, G. Myhre, V. Naik, K. P. Shine, B. Soden, G. Stenchikov, T. Storelvmo, Radiative forcing of climate: The historical evolution of the radiative forcing concept, the forcing agents and their quantification, and applications. *Meteorol. Monogr.* **59**, 14.1–14.101 (2019). doi:10.1175/AMSMONOGRAPHS-D-19-0001.1

7. M. G. Mlynczak, T. S. Daniels, D. P. Kratz, D. R. Feldman, W. D. Collins, E. J. Mlawer, M. J. Alvarado, J. E. Lawler, L. W. Anderson, D. W. Fahey, L. A. Hunt, J. C. Mast, The spectroscopic foundation of radiative forcing of climate by carbon dioxide. *Geophys. Res. Lett.* **43**, 5318–5325 (2016). doi:10.1002/2016GL068837 Medline

8. K. P. Shine, J. Cook, E. J. Highwood, M. M. Joshi, An alternative to radiative forcing for estimating the relative importance of climate change mechanisms. *Geophys. Res. Lett.* **30**, 2003GL018141 (2003). doi:10.1029/2003GL018141

9. J. Hansen, M. Sato, R. Ruedy, L. Nazarenko, A. Lacis, G. A. Schmidt, G. Russell, I. Aleinov, M. Bauer, S. Bauer, N. Bell, B. Cairns, V. Canuto, M. Chandler, Y. Cheng, A. D. Genio, G. Faluvegi, E. Fleming, A. Friend, T. Hall, C. Jackman, M. Kelley, N. Kiang, D. Koch, J. Lean, J. Lerner, K. Lo, S. Menon, R. Miller, P. Minnis, T. Novakov, V. Oinas, J. Perlwitz, J. Perlwitz, D. Rind, A. Romanou, D. Shindell, P. Stone, S. Sun, N. Tausnev, D. Thresher, B. Wielicki, T. Wong, M. Yao, S. Zhang, Efficacy of climate forcings. *J. Geophys. Res.* **110** (D18), D18104 (2005). doi:10.1029/2005JD005776

10. E.-S. Chung, B. J. Soden, An assessment of methods for computing radiative forcing in climate models. *Environ. Res. Lett.* **10**, 074004 (2015). doi:10.1088/1748-9326/10/7/074004

11. C. J. Smith, R. J. Kramer, G. Myhre, P. M. Forster, B. J. Soden, T. Andrews, O. Boucher, G. Faluvegi, D. Fläschner, Ø. Hodnebrog, M. Kasoar, V. Kharin, A. Kirkevåg, J.-F. Lamarque, J. Mülmenstädt, D. Olivié, T. Richardson, B. H. Samset, D. Shindell, P. Stier, T. Takemura, A. Voulgarakis, D. Watson-Parris, Understanding rapid adjustments to diverse forcing agents. *Geophys. Res. Lett.* **45**, 12023–12031 (2018). doi:10.1029/2018GL079826 Medline

12. C. J. Smith, R. J. Kramer, G. Myhre, K. Alterskjær, W. Collins, A. Sima, O. Boucher, J.-L. Dufresne, P. Nabat, M. Michou, S. Yukimoto, J. Cole, D. Paynter, H. Shiogama, F. M. O'Connor, E. Robertson, A. Wiltshire, T. Andrews, C. Hannay, R. Miller, L. Nazarenko, A. Kirkevåg, D. Olivié, S. Fiedler, R. Pincus, P. M. Forster, Effective radiative forcing and adjustments in CMIP6 models. *Atmos. Chem. Phys.* **20**, 9591–9618 (2020). doi:10.5194/acp-20-9591-2020

13. R. D. Cess, M.-H. Zhang, G. L. Potter, H. W. Barker, R. A. Colman, D. A. Dazlich, A. D. Del Genio, M. Esch, J. R. Fraser, V. Galin, W. L. Gates, J. J. Hack, W. J. Ingram, J. T. Kiehl, A. A. Lacis, H. Le Treut, Z.-X. Li, X.-Z. Liang, J.-F. Mahfouf, B. J. McAvaney, V. P. Meleshko, J.-J. Morcrette, D. A. Randall, E. Roeckner, J.-F. Royer, A. P. Sokolov, P. V. Sporyshev, K. E. Taylor, W.-C. Wang, R. T. Wetherald, Uncertainties in carbon dioxide radiative forcing in atmospheric general circulation models. *Science* **262**, 1252–1255 (1993). doi:10.1126/science.262.5137.1252 Medline

14. W. D. Collins, V. Ramaswamy, M. D. Schwarzkopf, Y. Sun, R. W. Portmann, Q. Fu, S. E. B. Casanova, J.-L. Dufresne, D. W. Fillmore, P. M. Forster, V. Y. Galin, L. K. Gohar, W. J. Ingram, D. P. Kratz, M.-P. Lefebvre, J. Li, P. Marquet, V. Oinas, Y. Tsushima, T. Uchiyama, W. Y. Zhong, Radiative forcing by well-mixed greenhouse gases: Estimates from climate models in the Intergovernmental Panel on Climate Change (IPCC) Fourth Assessment Report (AR4). *J. Geophys. Res.* **111**, D14317 (2006). doi:10.1029/2005JD006713

15. B. J. Soden, W. D. Collins, D. R. Feldman, Reducing uncertainties in climate models. *Science* **361**, 326–327 (2018). doi:10.1126/science.aau1864 Medline

16. N. Jeevanjee, J. T. Seeley, D. Paynter, S. Fueglistaler, An Analytical Model for Spatially Varying Clear-Sky CO_2 Forcing. *J. Clim.* **34**, 9463–9480 (2021). doi:10.1175/JCLI-D-19-0756.1

17. K. E. Taylor, R. J. Stouffer, G. A. Meehl, An overview of CMIP5 and the experiment design. *Bull. Am. Meteorol. Soc.* **93**, 485–498 (2012). doi:10.1175/BAMS-D-11-00094.1

18. V. Eyring, S. Bony, G. A. Meehl, C. A. Senior, B. Stevens, R. J. Stouffer, K. E. Taylor, Overview of the Coupled Model Intercomparison Project Phase 6 (CMIP6) experimental design and organization. *Geosci. Model Dev.* **9**, 1937–1958 (2016). doi:10.5194/gmd-9-1937-2016

19. R. Pincus, S. A. Buehler, M. Brath, C. Crevoisier, O. Jamil, K. F. Evans, J. Manners, R. L. Menzel, E. J. Mlawer, D. Paynter, R. L. Pernak, Y. Tellier, Benchmark Calculations of Radiative Forcing by Greenhouse Gases. *J. Geophys. Res. Atmos.* **125**, e2020JD033483 (2020). doi:10.1029/2020JD033483

20. X. Huang, X. Chen, C. Fan, S. Kato, N. Loeb, M. Bosilovich, S.-H. Ham, F. G. Rose, L. L. Strow, A synopsis of AIRS global-mean clear-sky radiance trends from 2003 to 2020. *J. Geophys. Res. Atmos.* **127**, e2022JD037598 (2022). doi:10.1029/2022JD037598

21. G. Myhre, E. Highwood, K. P. Shine, F. Stordal, New estimates of radiative forcing due to well mixed greenhouse gases. *Geophys. Res. Lett.* **25**, 2715–2718 (1998). doi:10.1029/98GL01908

22. M. Etminan, G. Myhre, E. J. Highwood, K. P. Shine, Radiative forcing of carbon dioxide, methane, and nitrous oxide: A significant revision of the methane radiative forcing. *Geophys. Res. Lett.* **43**, 12,614–12,623 (2016). doi:10.1002/2016GL071930

23. B. Byrne, C. Goldblatt, Radiative forcing at high concentrations of well-mixed greenhouse gases. *Geophys. Res. Lett.* **41**, 152–160 (2014). doi:10.1002/2013GL058456

24. R. Caballero, M. Huber, State-dependent climate sensitivity in past warm climates and its implications for future climate projections. *Proc. Natl. Acad. Sci. U.S.A.* **110**, 14162–14167 (2013). doi:10.1073/pnas.1303365110 Medline

25. W. Zhong, J. D. Haigh, The greenhouse effect and carbon dioxide. *Weather* **68**, 100–105 (2013). doi:10.1002/wea.2072

26. J. T. Seeley, "Convection, radiation, and climate: Fundamental mechanisms and impacts of a changing atmosphere," thesis, University of California, Berkeley (2018).

27. Y. Huang, X. Tan, Y. Xia, Inhomogeneous radiative forcing of homogeneous greenhouse gases. *J. Geophys. Res. Atmos.* **121**, 2780–2789 (2016). doi:10.1002/2015JD024569

28. D. M. Romps, J. T. Seeley, J. P. Edman, Why the forcing from carbon dioxide scales as the logarithm of its concentration. *J. Clim.* **35**, 4027–4047 (2022). doi:10.1175/JCLI-D-21-0275.1

29. K. P. Shine, R. G. Derwent, D. J. Wuebbles, J.-J. Morcrette, "Radiative forcing of climate," in *Climate Change: The IPCC Scientific Assessment* (Cambridge Univ. Press, 1990); pp. 41–68.

30. K. P. Shine, G. Myhre, The spectral nature of stratospheric temperature adjustment and its application to halocarbon radiative forcing. *J. Adv. Model. Earth Syst.* **12**, e2019MS001951 (2020). doi:10.1029/2019MS001951

31. I. Mitevski, L. M. Polvani, C. Orbe, Asymmetric warming/cooling response to CO2 increase/decrease mainly due to non-logarithmic forcing, not feedbacks. *Geophys. Res. Lett.* **49**, e2021GL097133 (2022). doi:10.1029/2021GL097133

32. C. M. Bitz, L. M. Polvani, Antarctic climate response to stratospheric ozone depletion in a fine resolution ocean climate model. *Geophys. Res. Lett.* **39**, 2012GL053393 (2012). doi:10.1029/2012GL053393

33. E. A. Barnes, N. W. Barnes, L. M. Polvani, Delayed Southern Hemisphere climate change induced by stratospheric ozone recovery, as projected by the CMIP5 models. *J. Clim.* **27**, 852–867 (2014). doi:10.1175/JCLI-D-13-00246.1

34. L. M. Polvani, M. Previdi, M. R. England, G. Chiodo, K. L. Smith, Substantial twentieth-century Arctic warming caused be ozone depleting substances. *Nat. Clim. Chang.* **10**, 130–133 (2020). doi:10.1038/s41558-019-0677-4

35. K. P. Shine, M. S. Bourqui, P. M. Forster, S. H. E. Hare, U. Langematz, P. Braesicke, V. Grewe, M. Ponater, C. Schnadt, C. A. Smith, J. D. Haigh, J. Austin, N. Butchart, D. T. Shindell, W. J. Randel, T. Nagashima, R. W. Portmann, S. Solomon, D. J. Seidel, J. Lanzante, S. Klein, V. Ramaswamy, M. D. Schwarzkopf, A comparison of model-simulated trends in stratospheric temperatures. *Q. J. R. Meteorol. Soc.* **129**, 1565–1588 (2003). doi:10.1256/qj.02.186

36. P. M. de Forster, K. P. Shine, Radiative forcing and temperature trends from stratospheric ozone changes. *J. Geophys. Res. Atmos.* **102**, 10841–10855 (1997). doi:10.1029/96JD03510

37. A. C. Maycock, W. J. Randel, A. K. Steiner, A. Y. Karpechko, J. Cristy, R. Saunders, D. W. J. Thompson, C. Z. Zou, A. Chrysanthou, N. L. Abraham, H. Akiyoshi, A. T. Archibald, N. Butchart, M. Chipperfield, M. Dameris, M. Deushi, S. Dhomse, G. Di Genova, P. Jöckel, D. E. Kinnison, O. Kirner, F. Ladstädter, M. Michou, O. Morgenstern, F. O. Connor, L. Oman, G. Pitari, D. A. Plummer, L. E. Revell, E. Rozanov, A. Stenke, D. Visioni, Y. Yamashita, G. Zeng, Revisiting the mystery of recent stratospheric temperature trends. *Geophys. Res. Lett.* **45**, 9919–9933 (2018). doi:10.1029/2018GL078035 Medline

38. M. F. Stuecker, C. M. Bitz, K. C. Armour, C. Proistosescu, S. M. Kang, S. P. Xie, D. Kim, S. McGregor, W. Zhang, S. Zhao, W. Cai, Y. Dong, F. F. Jin, Polar amplification dominated by local forcing and feedbacks. *Nat. Clim. Chang.* **8**, 1076–1081 (2018). doi:10.1038/s41558-018-0339-y

39. Q. Fu, S. Solomon, H. A. Pahlavan, P. Lin, Observed changes in Brewer-Dobson circulation for 1980–2018. *Environ. Res. Lett.* **14**, 114026 (2019). doi:10.1088/1748-9326/ab4de7

40. P. J. Durack, P. J. Gleckler, F. W. Landerer, K. E. Taylor, Quantifying underestimates of long-term upper-ocean warming. *Nat. Clim. Chang.* **4**, 999–1005 (2014). doi:10.1038/nclimate2389

41. D. Roemmich, J. Church, J. Gilson, D. Monselesan, P. Sutton, S. Wijffels, Unabated planetary warming and its ocean structure since 2006. *Nat. Clim. Chang.* **5**, 240–245 (2015). doi:10.1038/nclimate2513

42. J. E. A. Marshall, J. Lakin, I. Troth, S. M. Wallace-Johnson, UV-B radiation was the Devonian-Carboniferous boundary terrestrial extinction kill mechanism. *Sci. Adv.* **6**, eaba0768 (2020). doi:10.1126/sciadv.aba0768 Medline

43. I. H. Campbell, C. M. Allen, Formation of supercontinents linked to increases in atmospheric oxygen. *Nat. Geosci.* **1**, 554–558 (2008). doi:10.1038/ngeo259

44. M. R. Warke, T. Di Rocco, A. L. Zerkle, A. Lepland, A. R. Prave, A. P. Martin, Y. Ueno, D. J. Condon, M. W. Claire, The Great Oxidation Event preceded a Paleoproterozoic "snowball Earth". *Proc. Natl. Acad. Sci. U.S.A.* **117**, 13314–13320 (2020). doi:10.1073/pnas.2003090117 Medline

45. J. G. Shepherd, *Geoengineering the Climate: Science, Governance, and Uncertainty* (Royal Society, 2009); https://royalsociety.org/topics-policy/publications/2009/geoengineering-climate/.

46. A. Robock, Volcanic eruptions and climate. *Rev. Geophys.* **38**, 191–219 (2000). doi:10.1029/1998RG000054

47. D. T. Shindell, G. A. Schmidt, M. E. Mann, G. Faluvegi, Dynamic winter climate response to large tropical volcanic eruptions since 1600. *J. Geophys. Res.* **109** (D5), 2003JD004151 (2004). doi:10.1029/2003JD004151

48. P. J. Rasch, S. Tilmes, R. P. Turco, A. Robock, L. Oman, C.-C. Chen, G. L. Stenchikov, R. R. Garcia, An overview of geoengineering of climate using stratospheric sulphate aerosols. *Philos. Trans. A Math. Phys. Eng. Sci.* **366**, 4007–4037 (2008). doi:10.1098/rsta.2008.0131 Medline

49. A. J. Ferraro, E. J. Highwood, A. J. Charlton-Perez, Stratospheric heating by potential geoengineering aerosols. *Geophys. Res. Lett.* **38**, L24706 (2011). doi:10.1029/2011GL049761

50. B. Kravitz, A. Robock, D. T. Shindell, M. A. Miller, Sensitivity of stratospheric geoengineering with black carbon to aerosol size and altitude of injection. *J. Geophys. Res.* **117**, 2011JD017341 (2012). doi:10.1029/2011JD017341

51. M. G. Mlynczak, J. Yue, J. McCormack, R. S. Liebermann, N. J. Livesey, An observational gap at the edge of space. *Eos* **102**, (2021). doi:10.1029/2021EO155494

52. Data and code for: H. He, R. J. Kramer, B. J. Soden, N. Jeevanjee, State dependence of CO_2 forcing and its implications for climate sensitivity, Zenodo (2023); https://doi.org/10.5281/zenodo.10152455.

53. S. Bony, M. J. Webb, C. S. Bretherton, S. A. Klein, P. Siebesma, G. Tselioudis, M. Zhang, CFMIP: Towards a better evaluation and understanding of clouds and cloud feedbacks in CMIP5 models. *CLIVAR Exchanges* **56**, 20–22 (2011).

54. M. J. Webb, T. Andrews, A. Bodas-Salcedo, S. Bony, C. S. Bretherton, R. Chadwick, H. Chepfer, H. Douville, P. Good, J. E. Kay, S. A. Klein, R. Marchand, B. Medeiros, A. P. Siebesma, C. B. Skinner, B. Stevens, G. Tselioudis, Y. Tsushima, M. Watanabe, The Cloud Feedback Model Intercomparison Project (CFMIP) contribution to CMIP6. *Geosci. Model Dev.* **10**, 359–384 (2017). doi:10.5194/gmd-10-359-2017

55. R. Pincus, P. M. Forster, B. Stevens, The Radiative forcing model intercomparison project (RFMIP): Experimental protocol for CMIP6. *Geosci. Model Dev.* **9**, 3447–3460 (2016). doi:10.5194/gmd-9-3447-2016

56. T. Andrews, C. J. Smith, G. Myhre, P. M. Forster, R. Chadwick, D. Ackerley, Effective radiative forcing in a GCM with fixed surface temperatures. *J. Geophys. Res. Atmos.* **126**, e2020JD033880 (2021). doi:10.1029/2020JD033880

57. P. Good, T. Andrews, R. Chadwick, J.-L. Dufresne, J. M. Gregory, J. A. Lowe, N. Schaller, H. Shiogama, nonlinMIP contribution to CMIP6: model intercomparison project for non-linear mechanisms: physical basis, experimental design and analysis principles (v1.0). *Geosci. Model Dev.* **9**, 4019–4028 (2016). doi:10.5194/gmd-9-4019-2016

58. N. P. Gillett, H. Shiogama, B. Funke, G. Hegerl, R. Knutti, K. Matthes, B. D. Santer, D. Stone, C. Tebaldi, The Detection and Attribution Model Intercomparison Project (DAMIP v1.0) contribution to CMIP6. *Geosci. Model Dev.* **9**, 3685–3697 (2016). doi:10.5194/gmd-9-3685-2016

59. D. M. Lawrence, G. C. Hurtt, A. Arneth, V. Brovkin, K. V. Calvin, A. D. Jones, C. D. Jones, P. J. Lawrence, N. de Noblet-Ducoudré, J. Pongratz, S. I. Seneviratne, E. Shevliakova,

The Land Use Model Intercomparison Project (LUMIP) contribution to CMIP6: Rationale and experimental design. *Geosci. Model Dev.* **9**, 2973–2998 (2016). doi:10.5194/gmd-9-2973-2016

60. H. H. Aumann, M. T. Chahine, C. Gautier, M. D. Goldberg, E. Kalnay, L. M. McMillin, H. Revercomb, P. W. Rosenkranz, W. L. Smith, D. H. Staelin, L. L. Strow, J. Susskind, AIRS/AMSU/HSB on the Aqua mission: Design, science objectives, data products, and processing systems. *IEEE Trans. Geosci. Remote Sens.* **41**, 253–264 (2003). doi:10.1109/TGRS.2002.808356
61. H. T. Thrastarson, E. Manning, B. Kahn, E. J. Fetzer, Q. Yue, S. Wong, P. Kalmus, V. Payne, E. Olsen, R. C. Wilson, "AIRS/AMSU/HSB version 7 level 2 product user guide" (Jet Propulsion Laboratory, California Institute of Technology, 2020); https://docserver.gesdisc.eosdis.nasa.gov/public/project/AIRS/V7_L2_Product_User_Guide.pdf.
62. M. Schwartz, N. Livesey, W. Read, R. Fuller, "MLS/Aura Level 3 Monthly Binned Temperature on Assorted Grids V004" (NASA Goddard Earth Sciences Data and Information Services Center, 2020); https://doi.org/10.5067/AURA/MLS/DATA/3221.
63. M. Schwartz, N. Livesey, W. Read, R. Fuller, "MLS/Aura Level 3 Monthly Binned Temperature on Assorted Grids V005" (NASA Goddard Earth Sciences Data and Information Services Center, 2021); https://doi.org/10.5067/Aura/MLS/DATA/3550.
64. J. M. Russell III, M. G. Mlynczak, L. L. Gordley, J. J. Tansock Jr., R. W. Esplin, Overview of the SABER experiment and preliminary calibration results. *Proc. SPIE* **3756**, 277–288 (1999). doi:10.1117/12.366382
65. N. Smith, C. D. Barnet, Uncertainty characterization and propagation in the Community Long-term Infrared Microwave Combined Atmospheric Product System (CLIMCAPS). *Remote Sens.* **11**, 1227 (2019). doi:10.3390/rs11101227
66. H. Hersbach, B. Bell, P. Berrisford, S. Hirahara, A. Horányi, J. Muñoz-Sabater, J. Nicolas, C. Peubey, R. Radu, D. Schepers, A. Simmons, C. Soci, S. Abdalla, X. Abellan, G. Balsamo, P. Bechtold, G. Biavati, J. Bidlot, M. Bonavita, G. De Chiara, P. Dahlgren, D. Dee, M. Diamantakis, R. Dragani, J. Flemming, R. Forbes, M. Fuentes, A. Geer, L. Haimberger, S. Healy, R. J. Hogan, E. Hólm, M. Janisková, S. Keeley, P. Laloyaux, P. Lopez, C. Lupu, G. Radnoti, P. de Rosnay, I. Rozum, F. Vamborg, S. Villaume, J.-N. Thépaut, The ERA5 global reanalysis. *Q. J. R. Meteorol. Soc.* **146**, 1999–2049 (2020). doi:10.1002/qj.3803
67. R. Gelaro, W. McCarty, M. J. Suárez, R. Todling, A. Molod, L. Takacs, C. Randles, A. Darmenov, M. G. Bosilovich, R. Reichle, K. Wargan, L. Coy, R. Cullather, C. Draper, S. Akella, V. Buchard, A. Conaty, A. da Silva, W. Gu, G.-K. Kim, R. Koster, R. Lucchesi, D. Merkova, J. E. Nielsen, G. Partyka, S. Pawson, W. Putman, M. Rienecker, S. D. Schubert, M. Sienkiewicz, B. Zhao, The Modern-Era Retrospective Analysis for Research and Applications, Version 2 (MERRA-2). *J. Clim.* **30**, 5419–5454 (2017). doi:10.1175/JCLI-D-16-0758.1 Medline
68. M. Kanamitsu, W. Ebisuzaki, J. Woollen, S. K. Yang, J. J. Hnilo, M. Fiorino, G. L. Potter, NCEP-DOE AMIP-II reanalysis (R-2). *Bull. Am. Meteorol. Soc.* **83**, 1631–1644 (2002). doi:10.1175/BAMS-83-11-1631

69. J. M. Edwards, A. Slingo, Studies with a flexible new radiation code. I: Choosing a configuration for a large-scale model. *Q. J. R. Meteorol. Soc.* **122**, 689–719 (1996). doi:10.1002/qj.49712253107

70. J. Manners, J. M. Edwards, P. Hill, J.-C. Thelen, *SOCRATES (Suite Of Community RAdiative Transfer Codes Based on Edwards and Slingo) Technical Guide* (Met Office, 2015).

71. S. A. Buehler, J. Mendrok, P. Eriksson, A. Perrin, R. Larsson, O. Lemke, ARTS, the atmospheric radiative transfer simulator — Version 2.2, the planetary toolbox edition. *Geosci. Model Dev.* **11**, 1537–1556 (2018). doi:10.5194/gmd-11-1537-2018

72. D. D. B. Koll, T. W. Cronin, Earth's outgoing longwave radiation linear due to H_2O greenhouse effect. *Proc. Natl. Acad. Sci. U.S.A.* **115**, 10293–10298 (2018). doi:10.1073/pnas.1809868115 Medline

73. M. Meinshausen, E. Vogel, A. Nauels, K. Lorbacher, N. Meinshausen, D. M. Etheridge, P. J. Fraser, S. A. Montzka, P. J. Rayner, C. M. Trudinger, P. B. Krummel, U. Beyerle, J. G. Canadell, J. S. Daniel, I. G. Enting, R. M. Law, C. R. Lunder, S. O'Doherty, R. G. Prinn, S. Reimann, M. Rubino, G. J. M. Velders, M. K. Vollmer, R. H. J. Wang, R. Weiss, Historical greenhouse gas concentrations for climate modelling (CMIP6). *Geosci. Model Dev.* **10**, 2057–2116 (2017). doi:10.5194/gmd-10-2057-2017

74. T. Reichler, M. Dameris, R. Sausen, Determining the tropopause height from gridded data. *Geophys. Res. Lett.* **30**, 2003GL018240 (2003). doi:10.1029/2003GL018240

75. B. J. Soden, I. M. Held, R. Colman, K. M. Shell, J. T. Kiehl, C. A. Shields, Quantifying climate feedbacks using radiative kernels. *J. Clim.* **21**, 3504–3520 (2008). doi:10.1175/2007JCLI2110.1

76. C. J. Smith, R. J. Kramer, A. Sima, The HadGEM3-GA7.1 radiative kernel: The importance of a well-resolved stratosphere. *Earth Syst. Sci. Data* **12**, 2157–2168 (2020). doi:10.5194/essd-12-2157-2020